A Practical Current Source Inverter-Based High-Power Medium-Voltage PV System

Ling Xing, Qiang Wei, *Senior Member, IEEE*, and Yunwei Li, *Fellow, IEEE*

***Abstract*—The power converters currently used in high-power (a few megawatts) medium-voltage PV systems require the use of a line-frequency transformer (LFT), which is bulky and costly. To solve this issue, cascaded H-bridge converter and modular multilevel converter based converters were proposed and investigated in the literature. They can eliminate the LFT but suffer several technical challenges, one of which, for example, is a power imbalance. To address these challenges, extra efforts, such as modified converters, modulations, and controls, are needed. Such extras burden the original converters and introduce new challenges. Therefore, a new power converter is proposed in this work. It eliminates the LFT without these challenges faced by the existing solutions. In addition, it features reliable short-circuit protection, high scalability, simple, and well-proven converters. The operation principle is introduced, and the control scheme is developed. The performance is investigated and verified based on both simulations and lab-scaled experiments.**

***Index Terms*—High-power converter, medium-voltage (MV), power imbalance, PV system.**

I. Introduction

Fig. 1 shows the typical configuration of commercial high-power (a few megawatts) medium-voltage (MV) PV systems [1]. Due to the insulation limit of PV panels, a maximum dc voltage of up to 1500 V is built with series/parallel-connected solar panels. As a result, a line-frequency transformer (LFT) is required and used to boost the generated low voltage to MV levels and then connected to the MV grid. The conventional two-level/three-level voltage source inverters (VSIs) are employed to build the central inverters/string inverters. Several such inverters are connected in parallel through a multiwinding LFT to reach higher power ratings.

To eliminate the LFT, high-power MV converters have been considered a good candidate. Different MV converters have been developed and investigated, among which the cascaded H-bridge converters (CHB) and modular multilevel converters (MMC) are considered the most promising converters for the high-power

Manuscript received 16 May 2022; revised 10 August 2022; accepted 28 September 2022. Date of publication 3 October 2022; date of current version 18 November 2022. Recommended for publication by Associate Editor K. A. Kim. *(Corresponding author: Qiang Wei.)*

Ling Xing and Yunwei Li are with the Electrical and Computer Engineering, University of Alberta, Edmonton, AB T6G 2R3, Canada (e-mail: lxing1@ualberta.ca; yunwei.li@ualberta.ca).

Qiang Wei is with the Electrical Engineering, Lakehead University, Thunder Bay, ON P7B 5E1, Canada (e-mail: qwei@lakeheadu.ca).

Color versions of one or more figures in this article are available at https://doi.org/10.1109/TPEL.2022.3211409.

Digital Object Identifier 10.1109/TPEL.2022.3211409

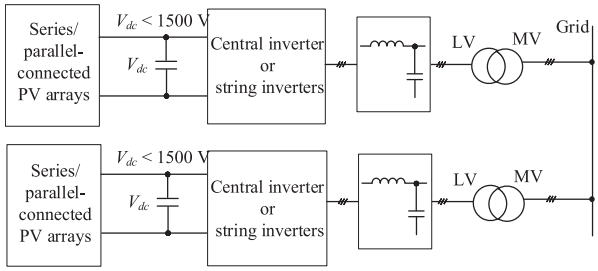

Fig. 1. Configuration of high-power MV PV systems [1].

PV system [2], [3], [4], [5], [6], [7], [8], [9], [10], [11], [12], [13], [14], [15], [16], [17], [18], [19], [20], [21], [22], [23], [24], [25], [26]. They feature high-efficient maximum power point tracking (MPPT), high modularity and scalability, etc., while they also have a few technical challenges, one of which, for example, is a power imbalance. To address these challenges, modified converters, new modulations, and advanced controls have been proposed and investigated. In the following, they will be introduced in detail.

The existing CHB-based PV converters can be classified into three categories: CHB with separate PV modules, as shown in Fig. 2(a) [2], [3], [4], [5], [6], [7], [8], [9], [10], [11], [12], [13], [14], CHB with common ac link, as shown in Fig. 2(b) [15], [16], [17], [18], and CHB with common dc link, as shown in Fig. 2(c) [19], [20], [21], [22]. The one with separate PV modules can achieve distributed MPPT but suffers intermodule and interphase power mismatch, as well as poor output harmonics performance under partial shading conditions [6], [7], [8], [9], [10], [11], [12], [13], [14]. Modified converters, modulations, and controls have been developed to alleviate such issues, although the imbalance issue cannot be eliminated [6], [7], [8], [9], [10], [11], [12], [13], [14]. The CHB with a common ac link, as shown in Fig. 2(b), also ensures distributed MPPT. In addition, it provides a common ac link for the CHB inverter, and as a result, the power imbalance issue due to the nonuniform solar irradiance conditions is solved. But this converter introduces a couple of new challenges [15], [16], [17], [18]: one is voltage/power imbalance caused by parameter mismatch of the high-power medium/high-frequency multiwinding transformers, second, the manufacturing of high-power high-frequency multiwinding transformers is a burden, and third, it requires more power conversion stages resulting in lower efficiency. Fig. 2(c) shows the version with a common dc link in which the distributed MPPT is ensured by using separate MPPT converters

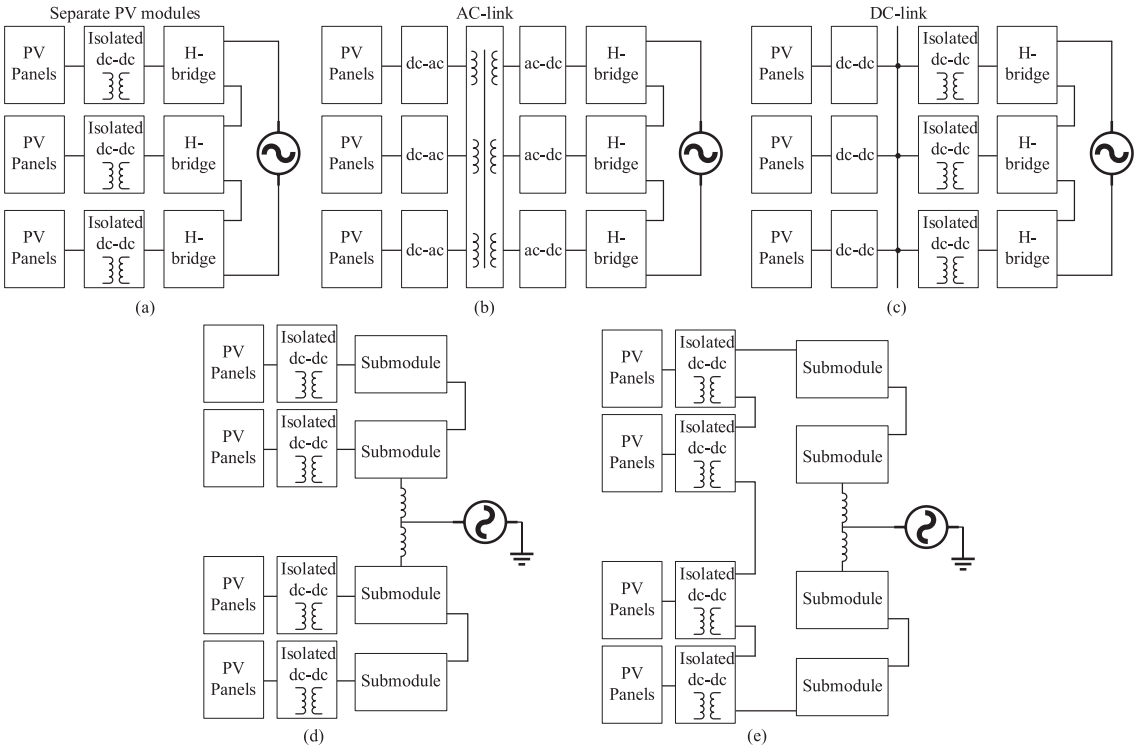

Fig. 2. Configuration of CHB- and MMC-based PV converters—single phase.

and the imbalance issue is addressed by sharing the dc link of the CHB inverter. However, as same as the previous one, this version suffers a high number of power conversion stage, which lowers conversion efficiency. And power/voltage imbalance may be introduced by the parameter mismatch of used high-frequency transformers. Furthermore, for the three versions, the number of operating power cells per phase should be the same. To do so, the corresponding healthy power cells in healthy phases need to be bypassed as same as the faulty ones under faults.

The existing MMC-based PV converters can be similarly classified into MMC with separate PV modules, as shown in Fig. 2(d) [23], [24], and MMC with a common dc link, as shown in Fig. 2(e) [25], [26]. The MMC with the common dc link consists of series-connected PV converters to form an MVDC level and then connected to a conventional MMC. Different isolated dc–dc converters can be used in this converter as discussed in [27], [28], [29], [30], and [31]. The use of isolated dc–dc converters and the provision of the common dc link allow both independent MPPT and power balancing. However, since the dc-link voltage must be constant and the voltage balancing of PV converters must be ensured in the full operation range, expensive redundancy and overrating of converters must be introduced to ensure a reliable operation. For example, once one PV converter is failed and bypassed, the healthy ones must be able to withstand the same dc-link voltage to enable a continued operation of the PV system. The MMC with separate PV modules is similar to its CHB counterpart that it suffers power imbalance under inconsistent solar irradiance conditions and requires extra effort [32], [33].

To sum up, the existing solutions can eliminate the LFT but have one or some of the following challenges: power imbalance, low MPPT efficiency, large power conversion stage, high manufacturing burden, complex control, and expensive redundancy design and overrating.

Therefore, with the motivation for developing a practical high-power MV converter without the use of LFT and without the challenges, a new converter is proposed. It consists of separate PV-side converters connected in series to reach an MV level and then connected to an MV current source inverter (CSI). It eliminates the LFT and solves all these challenges faced by the existing solutions, and in addition, it features reliable short-circuit protection, high scalability, simple, and well-proven converters. The control scheme for the proposed converter is developed. The performance is verified by both simulation and experiments.

II. Proposed CSI-Based PV Converter

A. Operation Principle

Fig. 3 shows the proposed CSI-based converter. At the PV side, identical dc–dc converters are used to achieve independent MPPT for the corresponding PV panels. The used dc–dc converters are the well-studied isolated H-bridge converters used in the existing CHB/MMC-based converters. The outputs of the isolated dc–dc converters are connected in series to reach an MVDC level to accommodate the use of the grid-side MV inverter. At the grid side, the well-proven MV CSI is used. It is composed of six (symmetrical GCT) SGCT devices with a reverse voltage blocking capability. Each of these devices can be replaced with two or more devices in series for higher voltage applications. For example, in the case of grid voltage

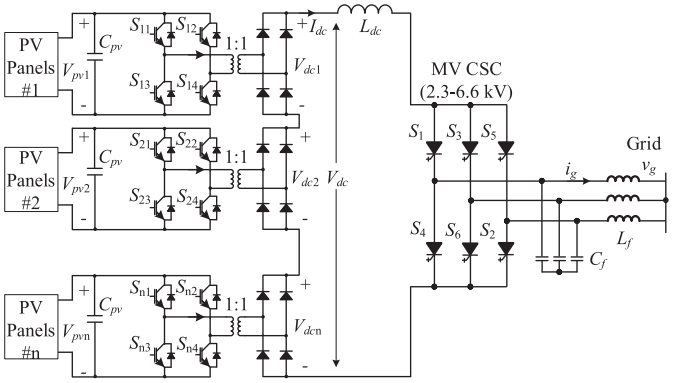

Fig. 3. Proposed CSC-based converter for MV high-power PV systems.

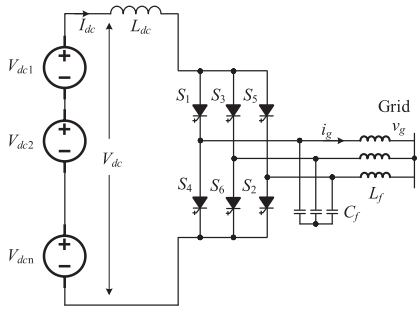

Fig. 4. Simplified equivalent circuit of the proposed converter.

of 2300 V, 2 SGCTs are needed for each phase, and for grid voltage of 3300, 4160, and 6600 V, the required number of devices per phase is 4, 4, and 6, respectively. The MV CSI is a well-proven inverter in high-power MV (2.3–6.6 kV) drives [34], and there is no technical challenge that arises when transferred to the high-power PV systems. On the other hand, the MV CSI features a simple topology, grid friendly waveform, and reliable short-circuit protection.

The rated number (n) of isolated dc–dc converters, the same as that of the PV panel sets, as shown in Fig. 3, is determined by the following:

1) the dc-link voltage $V_{\rm dc}$;
2) the device rating; and
3) the solar conditions.

For example, for a 1 MW/4160 V system, $V_{\rm dc}$ is around 5000 V that can be formed with different combinations of switch rating and number n. One is 1200 V IGBT, $V_{{\rm pv}n} = 700$ V (hard switching), $V_{{\rm dc}n} = 630$ V (rated duty cycle of the H-bridge converter $d = 0.45$), and n is then rounded to $n = 8$. And, it can also be 600 V IGBT, $V_{{\rm pv}n} = 400$ V (hard switching), $V_{{\rm dc}n} = 360$ V (rated duty cycle of the H-bridge converter $d = 0.45$), and n is then rounded to $n = 14$. The solar condition should also be considered. To ensure MPPT for all panel sets, a higher number n is preferred if the mismatch in solar irradiance is significant, while less number n would be fine under well-balanced solar irradiance. To sum up, the optimization of n is an engineering question in which a tradeoff is required. Such optimization is not a focus in this work.

The passive components used in the proposed converter are designed in the same manner as the existing ones. The used transformer here plays one role, that is isolating the PV panels from MVDC and by doing so, such as existing CHB-based solutions, the LFT can be eliminated without causing insulation issue for the PV panels. On this basis, the turn ratio of the used transformer is set to 1:1. The turn ratio also affects the design of n, but is also an engineering question as discussed earlier, thus not discussed here. The PV capacitors $C_{\rm pv}$ are selected based on the voltage ripple as well as the switching frequency, refer to the articles presented in [2], [3], [4], [5], [6], [7], [8], [9], [10], [11], [12], [13], and [14] for details. The dc-link inductor $L_{\rm dc}$ is designed based on the voltage-second principle and the *LC* filter is designed according to the grid codes. For example, under a switching frequency of around 500 Hz and a typical switching frequency for high-power MV CSI, $L_{\rm dc} = 0.8$ p.u., $L_f = 0.1$ p.u., and $C_f = 0.5$ p.u. are used. Refer to the articles presented in [34], [35], [36], [37], [38], and [39] for more details of CSI.

Each PV-side dc–dc converter is operating independently. As a result, MPPT is achieved for all the PV panels and the control of each dc–dc converter is independent. The resultant equivalent circuit of the proposed converter is derived and shown in Fig. 4. The PV-side dc–dc converters share one dc current $I_{\rm dc}$, while they may have different input/output voltages due to the different MPPTs at different PV panels. As shown in the figure, $V_{\rm dc1}$ and $V_{{\rm dc}n}$ are the obtained output voltages of the dc–dc converters #1 and #n, respectively, upon their respective MPPT. Since different PV panels may have different MPPTs, $V_{\rm dc1} \neq V_{{\rm dc}n}$ is the fact. This is not allowed in the MMC-based converters with a common dc link in which a constant $V_{\rm dc}$, as well as a balanced voltage of $V_{\rm dc1} = V_{{\rm dc}n}$, is a must under all conditions [25], [26]. But in the proposed converter, it is allowed since the proposed CSI-based converter is operating with a variable dc voltage $V_{\rm dc}$ ranging from 0 to 1 p.u. An extreme case is that when one or some of the PV-side converters are bypassed due to reasons, such as failure and shading, the left healthy converters continue to operate under a new operating point without balancing/voltage controls and without overvoltage and voltage imbalance issues. Note that the bypass operation can be implemented by the diode rectifier of the dc–dc converters, as shown in Fig. 3. Therefore, no voltage balancing control is required, and no overrating/redundancy is needed. In addition, the use of single grid-side CSI does not have the power imbalance issue that existed in the CHB- and MMC-based converters.

B. Comparison and Discussion

The comparison between the proposed converter and existing ones is discussed as follows and given in Table I. Note that the comparison between existing ones has been done well in [32] and [33], thus not repeated here.

LFT: The same as the CHB- and MMC-based ones, the proposed converter eliminates the LFT.

MPPT: The same as the CHB- and MMC-based ones, the proposed converter achieves independent MPPT due to the use of independent dc–dc converters.

Voltage imbalance: Such as the CHB- and MMC-based ones, the use of independent MPPT results in voltage imbalance. But such voltage imbalance is normal for the proposed converter,

TABLE I
COMPARISON OF DIFFERENT CONVERTERS FOR MV PV SYSTEMS

Items	CHB			MMC		Proposed converter
	CHB-1, Fig. 2 (a)	CHB-2, Fig. 2 (b)	CHB-3, Fig. 2 (c)	MMC-1, Fig. 2 (d)	MMC-2, Fig. 2 (e)	
LFT	No	No	No	No	No	No
Independent MPPT	Yes	Yes	Yes	Yes	Yes	Yes
Power imbalance issue	Yes	Yes*	Yes*	Yes	No	No
Voltage imbalance issue	Yes	Yes*	Yes*	Yes	No	No
Mismatch tolerance	Yes	No	No	Yes	Yes	Yes
Overrating/redundancy	No	No	No	No	Yes	No
Power conversion stage	Less	More	More	Less	More	Less
Short-circuit protection	No	No	No	No	No	Yes
Scalability	High	Low [32]	High	High	High	High
*: Introduced by parameter mismatch, not by partial shading.						

which is operating with a variable dc-link voltage, not a constant one. Each PV-side converter ($V_{\mathrm{dc}n}$) and the dc-link voltage (V_{dc}) can be ranging from 0 to 1 p.u.

Power imbalance: The voltage imbalance results in a power imbalance between PV-side dc–dc converters. Unlike the CHB- and MMC-based ones, the imbalance is not an issue for the grid-side waveforms due to the MV dc link.

Parameter mismatch: Parameter mismatches exist, but unlike the CHB- and MMC-based ones in which imbalances are introduced by the mismatches, the proposed converter tolerates these imbalances, as analyzed earlier.

Overrating and redundancy design: Unlike existing ones, the proposed converter does not need overrating or redundancy design. The failed PV-side converters if any are just bypassed without causing overvoltage issues.

Others: The proposed one inherits all the advantages of the MV CSI, such as simple topology and reliable short-circuit protection. In addition, such as the CHB- and MMC-based ones, it features high scalability and well-proven converters.

C. Challenge and Solution

The proposed CSI-based converter also inherits the challenge associated with the MV CSI, that is the bulky and less-efficient dc-link inductor.

The dc-link inductor and ac-side *LC* filter of the proposed CSI-based system are analogous to the dc-link capacitor and ac-side *LCL* filter of the existing VSI-based system in which the LFT is used, as shown in Fig. 1. Since the exact physical sizes of these passive components in the two inverters under the same conditions are unavailable, it is difficult to determine the difference if any between the two physical sizes. But the difference if any would not be large enough to offset the size reduction due to the elimination of the LFT of the proposed converter because these passive components used in the existing VSI-based systems are also bulky, and the LFT is very bulky. On the other hand, the proposed converter is expected to have a significant size reduction due to the elimination of the LFT.

The physical size of the proposed system can be further reduced by reducing the used passive components. The commercial high-power MV CSI equipped with the switch of SGCT is operating with a switching frequency of around 500 Hz to lower power losses. The development of SiC/GaN switches with higher switching frequencies and lower power losses enables the CSI-based system to reduce the passive components significantly [41]. In addition, the physical size of the dc-link inductor can be further reduced by coupled inductor design and reduced dc-link current. The dc-link inductance is theoretically halved by using the coupled inductor design. For a given power rating, the rated dc-link current can be reduced by increasing the rated dc-link voltage.

The estimated efficiency of the proposed converter is around 96% in which the MV CSI is 99%, the dc-link inductor is 98%, and the H-bridge converter 99% [34]. The efficiency of most existing LFT-based high-power PV systems is ranging from 95.6% to 96.9% in which the typical efficiency of the high-power LFT is around 98.5%, and the inverter ranges from 97.1% to 98.4% under rated conditions (higher efficiencies are reached under light loads), refer to examples, such as PVS980 and ULTRA-1500.0-TL manufactured by ABB and SG5000UD/SG5000UD-20 manufactured by Sungrow.

The efficiency of the proposed system can be also further improved by the methods, as analyzed earlier, and in addition, the variable dc-link current control allows a further efficiency improvement in the full operation range [34].

III. CONTROL SCHEME FOR THE PROPOSED CONVERTER

Fig. 5 shows the proposed control scheme for the proposed converter. It includes PV-side control and grid-side control.

A. PV-Side Control

The PV-side converter controls MPPT. Existing MPPT schemes can be used here and will not be discussed. As shown in Fig. 5, the reference voltage $V_{\mathrm{pv}n\text{-ref}}$ is received based on the respective MPPT of each PV set. The reference voltage is compared with the measured voltage and the error is going through a PI controller, which generates the reference current $i_{\mathrm{dc\text{-}ref}n}$. The required duty cycle d_n for PV set #*n* to ensure MPPT is then obtained by dividing the reference current $i_{\mathrm{dc\text{-}ref}n}$ by the dc current i_{dc}. The dc current i_{dc} is shared by all the PV-side converters and, therefore, under different solar conditions, different voltages' references ($V_{\mathrm{pv1\text{-}ref}} \neq V_{\mathrm{pv}n\text{-ref}}$) will be generated, which generate different current references ($i_{\mathrm{dc\text{-}ref1}} \neq i_{\mathrm{dc\text{-}ref}n}$) outputting different duty cycles ($d_1 \neq d_n$) for different PV converters. MPPT is achieved upon applying d_n.

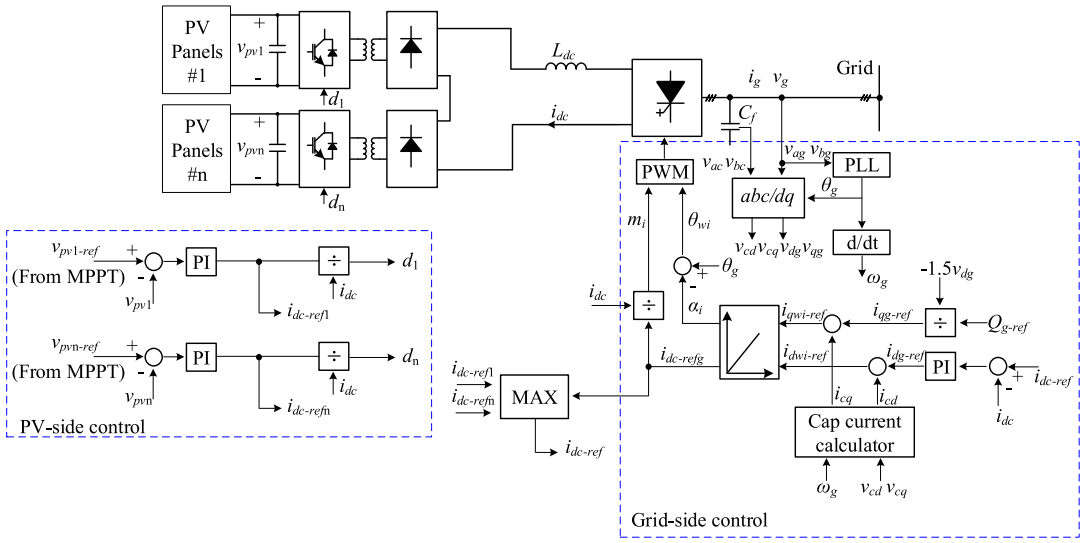

Fig. 5. Proposed control scheme for the proposed converter.

B. Grid-Side Control

The grid-side controls include dc current control and reactive power control, as shown in Fig. 5. The two controls are independently implemented in the *dq* frame. The *d*-axis grid current reference ($i_{dg\text{-ref}}$) is obtained by the dc current PI controller. The *q*-axis grid current reference ($i_{qg\text{-ref}}$) is obtained based on the reactive power reference ($Q_{g\text{-ref}}$) and the *d*-axis grid voltage (v_{dg}) [40]

$$\begin{aligned} P_g &= \tfrac{3}{2} v_{dg} i_{dg} \\ Q_g &= -\tfrac{3}{2} v_{dg} i_{qg}. \end{aligned} \tag{1}$$

The capacitor currents of the CSI need to be compensated in finalizing the references for the *dq*-axis pulsewidth modulation (PWM) currents ($i_{dwi\text{-ref}}$ and $i_{qwi\text{-ref}}$). The relationship among capacitor currents, grid currents, and the PWM currents is given as follows [40]:

$$\begin{aligned} i_{dwi-\text{ref}} &= i_{dg-\text{ref}} - i_{cd} = i_{dg-\text{ref}} + \omega_g C_f v_{cq} \\ i_{qwi-\text{ref}} &= i_{qg-\text{ref}} - i_{cq} = i_{qg-\text{ref}} - \omega_g C_f v_{cd} \end{aligned} \tag{2}$$

where ω_g is the grid frequency, i_{cd} and i_{cq} are the *dq*-axis capacitor currents, and v_{cd} and v_{cq} are the *dq*-axis capacitor voltages. These variables are related to the following [40]:

$$\begin{aligned} v_{cd} &= V_{sd} - \omega_g L_f i_{sq} \\ v_{cq} &= \omega_g L_f i_{sd} \end{aligned} \tag{3}$$

where L_f and ω_g are the filter inductor and angular speed of the grid, respectively.

Then, the required dc current reference ($i_{\text{dc-ref}g}$) and delay angle (α_i) of the grid-side CSI to ensure grid-side controls can be obtained according to Cartesian-to-polar transformation

$$\begin{aligned} i_{\text{dc}-\text{ref}g} &= \sqrt{(i_{dwi-\text{ref}})^2 + (i_{qwi-\text{ref}})^2} \\ \alpha_i &= \tan^{-1}(i_{qwi-\text{ref}} / i_{dwi-\text{ref}}). \end{aligned} \tag{4}$$

The required modulation index (m_i) for the CSI is then calculated by dividing the generated PWM current reference ($i_{\text{dc-ref}g}$) by the measured dc current i_{dc}. And the required angle of the PWM current (θ_{wi}) is calculated based on $\theta_{wi} = \theta_g - \alpha_i$ in which θ_g is the grid voltage angle obtained based on the phase-locked loop. After applying m_i and θ_{wi} to the grid-side converter with a conventional modulation scheme [35], [36], [37], [38], [39], both reactive power and dc current controls are achieved.

C. DC Current Reference Determination

The dc current reference is determined by the controls at both PV and grid sides. The PV-side control generates the PV-side reference, that is $i_{\text{dc-ref1}}$ for PV #1 and $i_{\text{dc-ref}n}$ for PV #*n*. Similarly, the grid-side controls generate the grid-side reference $i_{\text{dc-ref}g}$. In the proposed converter with a series-connected structure in which there is only one dc current flowing through all the converters, there is only one dc current reference. To ensure controls at both sides, the maximum value of all the references generated at both sides is selected to be the final dc current reference, that is

$$i_{\text{dc}-\text{ref}} = \max\{i_{\text{dc}-\text{ref1}}, i_{\text{dc}-\text{ref}n}, i_{\text{dc}-\text{ref}g}\} \tag{5}$$

where the PV-side references $i_{\text{dc-ref1}}$ and $i_{\text{dc-ref}n}$ are inversely proportional to the transformer turn ratio (1:*k*; in this case $k = 1$). Therefore, in cases where the PV-side references are larger than the grid-side reference resulting in a higher final dc reference under rated conditions, the transformer turn ratio can be designed in such a way that the references at both sides are the same. By doing so, the final dc reference is reduced.

The dc reference is expected to be as small as possible to lower power losses. To do so, the modulation index of the grid-side CSI is set to 1 [40].

The PV-side dc current reference is calculated as follows:

$$i_{\text{dc}-\text{ref}n} = \frac{P_n}{2 d_n V_{\text{pv}n}} \tag{6}$$

where P_n is the captured power for PV set #*n*.

TABLE II
SIMULATION AND EXPERIMENTAL PARAMETERS

Parameters	Simulation	Experiment
Nominal power	1 MW	600 W
Grid voltage, V_g	4160 V	104 V
PV-side converter		
# of converters, n	3	2
Nominal PV voltage, v_{pvn}	2000 V	70 V
PV capacitor, C_{pv}	100 μF	1000 μF
Switching frequency	1.2 kHz	1.2 kHz
Grid-side converter		
DC inductor, L_{dc}	45 mH	45 mH
Filter inductor, L_f	5 mH	5 mH
Filter capacitor, C_f	70 μF	100 μF
Switching frequency	540 Hz	540 Hz
Modulation scheme	SVM	SVM

Assuming a lossless system, the grid-side dc current reference can be received by combining (1)–(4) (7) shown at the bottom of this page.

IV. SIMULATED AND EXPERIMENTAL INVESTIGATION

Both simulations and lab-scaled experiments are conducted to verify the performance of the proposed converter and the performance of the proposed control. The used parameters are listed in Table II.

A. Simulated Results

Fig. 6 shows the simulated waveforms of the proposed converter under different conditions.

$1 < t < 1.5$ s: The converter is operating under rated conditions. Capacitor voltages $v_{\rm pv1}$, $v_{\rm pv2}$, and $v_{\rm pv3}$ of the PV-side converters #1, #2, and #3 are controlled to be at their reference values $v_{\rm pv1\text{-}ref}$, $v_{\rm pv2\text{-}ref}$, and $v_{\rm pv3\text{-}ref}$ received from MPPT. This indicates that MPPT is achieved for all the PV sets. The grid-side controls, including both dc-link current control and reactive power control, are also achieved. The real power (P_g) and reactive power (Q_g) are 1 p.u. and 0 p.u., respectively, and the dc-link current ($i_{\rm dc}$) is controlled to be 1 p.u. At $t = 1.5$ s, the reference voltage ($v_{\rm pv1\text{-}ref}$) for PV converter #1 is set at 1 p.u. still, while the references for PV converters #2 and #3 are reduced to 0.8 p.u. and 0.6 p.u., respectively. This is to simulate the nonuniform solar irradiance situation in practice. $v_{\rm pv1}$, $v_{\rm pv2}$, and $v_{\rm pv3}$ are well tracking their respective references. And the same for the dc-link current control. $Q_{g\text{-ref}}$ is set to 0.

$1.5 < t < 2.5$ s: The converter is operating with a new operating point at which $v_{\rm pv1}$, $v_{\rm pv2}$, and $v_{\rm pv3}$ are operating at 1 p.u., 0.8 p.u., and 0.6 p.u. following their respective references. P_g is reduced from 1 to 0.8 p.u. accordingly, while Q_g remains the same at 0. The resultant dc-link current ($i_{\rm dc}$) is operating at its new reference ($i_{\rm dc\text{-}ref}$). Compared with the previous period, the new reference is reduced to 0.83 p.u., and as analyzed earlier, this is to ensure control objectives on both sides as well as lowering the power loss of the converter. At $t = 2.5$ s, the reference voltages ($v_{\rm pv1\text{-}ref}$ and $v_{\rm pv2\text{-}ref}$) for PV converters #1 and #2 remain the same as before, while the reference for PV converter #3 is reduced to 0 p.u. This is to simulate the extreme case, under which converter #3 is bypassed under faults. In the simulation, this is done by setting the input power of converter #3 to 0. $v_{\rm pv3}$ is tracking the new reference well, and a new dc reference is generated to lower the power loss as well as ensuring control objectives at both sides.

$2.5 < t < 3.5$ s: The converter is operating with a new operating point at which $v_{\rm pv1}$, $v_{\rm pv2}$, and $v_{\rm pv3}$ are operating at 1 p.u., 0.8 p.u., and 0 p.u. P_g is further reduced from 0.8 to 0.6 p.u., while Q_g remains at 0. $i_{\rm dc}$ is operating with its new reference ($i_{\rm dc\text{-}ref}$), reduced from 0.83 to 0.79 p.u. Note that the reduction of the dc current reference is not proportional to that of the power and this is due to the capacitor current that needs to be compensated, as shown in (7). At $t = 3.5$ s, all the references are set back to 1 p.u., and Q_g remains at 0.

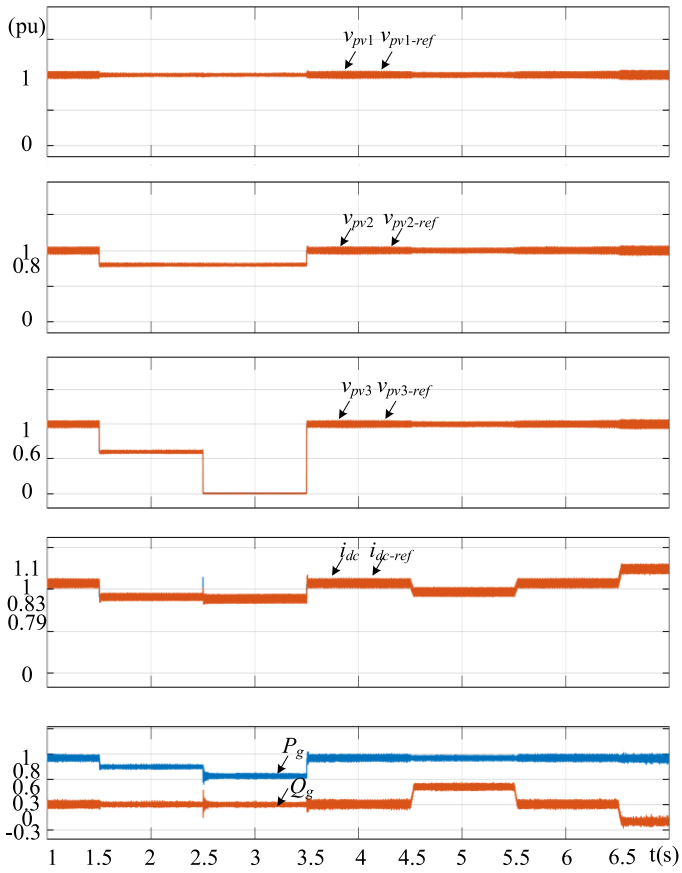

Fig. 6. Simulated performance under both steady and dynamic states.

$$I_{\rm dc\_ref}{}_g = \sqrt{\left\{(1-\omega_g^2 L_g C_f)\left(\frac{2}{3}\frac{\sum_{n=1}^{n} P_n}{V_{dg}}\right)\right\}^2 + \left\{(1-\omega_g^2 L_g C_f)\left(\frac{2}{3}\frac{Q_{g\_\rm ref}}{V_{dg}}\right) + \omega_g C_f V_{dg}\right\}^2}. \quad (7)$$

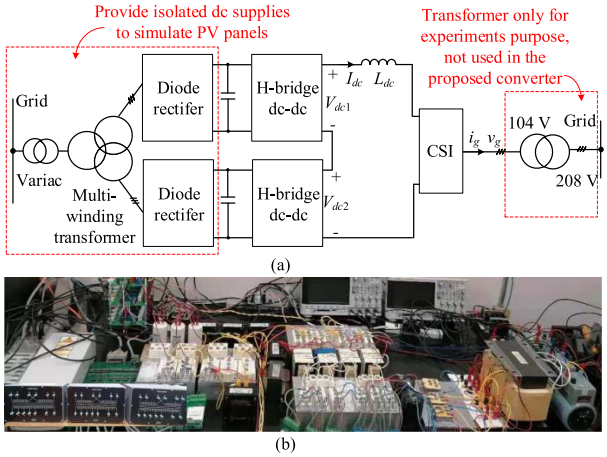

Fig. 7. Experimental setup. (a) Circuit. (b) Photograph.

$3.5 < t < 4.5$ s: The converter is operating in a rated steady state, the same as the period of $1 < t < 1.5$ s. At $t = 4.5$ s, the reference voltages are the same as before, while $Q_{g\text{-ref}}$ is set to 0.33 p.u. corresponding to a lagging power factor of 0.95. As shown in the figure, a new dc-link current reference ($i_{\text{dc-ref}}$) is generated following the change in reactive power.

$4.5 < t < 5.5$ s: The converter is operating with a new operating point at which v_{pv1}, v_{pv2}, v_{pv3}, and P_g are operating all at 1 p.u., while Q_g is settling down at 0.33 p.u. The resultant dc-link current (i_{dc}) is operating at its new reference ($i_{\text{dc-ref}}$), around 0.9 p.u. to accommodate the change in reactive power. At $t =$ 5.5 s, the references are set to the original values.

$5.5 < t < 6.5$ s: The converter is operating with the original rated conditions. At $t = 6.5$ s, the reference voltages are the same as the previous, while $Q_{g\text{-ref}}$ is set to -0.33 p.u. corresponding to a leading power factor of 0.95. As shown in the figure, the dc-link current reference ($i_{\text{dc-ref}}$) is increased from 1 p.u. to around 1.1 p.u. The relationship between the dc-link current reference and reactive power can be found in (7).

$6.5 < t < 7$ s: The converter is operating with a new operating point at which v_{pv1}, v_{pv2}, v_{pv3}, and P_g are operating all at 1 p.u., while Q_g is controlled to be at its new reference -0.33 p.u. The resultant i_{dc} is tracking its new reference (1.1 p.u.). And the PV-side control is achieved by the control of the three converters independently as indicated by v_{pv1}, v_{pv2}, and v_{pv3}.

B. Experimental Results

Fig. 7 shows the following experimental setup.

1) Variac + multiwinding transformer + diode rectifier is used at the PV side to provide isolated dc supplies to simulate the PV panels.
2) Two PV converters are used due to the limit of the available multiwinding transformer.
3) Since the use of a diode rectifier does not allow the control of PV capacitor voltages as in the simulation, an open-loop control is used for the PV-side converters. It is worth noting that the well-proven MPPT schemes are not studied here, while the focus is on the power converter, and therefore, the variac + multiwinding transformer + diode rectifier is used to provide independent dc voltages to simulate independent PV panels in practice. This simplification still allows the outputs (one is the duty cycle required for MPPT and the other the PV-side reference current, as shown in Fig. 5) to be generated and, therefore, is effective in verifying the proposed converter.
4) A transformer is purposely used at the grid side to lower the grid voltage to facilitate grid connection, but it is not needed for this proposed converter.

Fig. 8(a) shows the experimental waveforms of the proposed converter under rated conditions. The two output voltages of the PV-side converters (v_{dc1} and v_{dc2}) are around 50 V. Note that v_{dc1} is not equal to v_{dc2} and this is due to the mismatch of the used medium-frequency transformers of the H-bridge converters. The dc-link current (i_{dc}) is 6 A, and the grid voltage ($v_{g,L\text{-}L}$) and grid current (i_g) are 104 V and 3.2 A. The line-to-line grid voltage leads the grid current by 30°, and this indicates a unity power factor (PF = 1).

Fig. 8(b) shows the experimental waveforms of the proposed converter under a dynamic state with a lagging power factor (PF = 0.95 lagging). Before the lagging power factor control is activated, the converter is operating with a unity power factor as same as that in Fig. 8(a), and after that, the reactive power (0.33 p.u.) control is enabled, while the real power is unchanged. As a result, the peak value of the grid current (i_g) is slightly increased from around 4.5–4.8 A and its phase angle is lagging the line-to-line voltage of the grid by 48°. Unlike the simulation in which the dc current (i_g) is reduced during the lagging power factor control, i_{dc} does not change in the experiments. This is because the PV-side current reference is greater than the grid-side one in the experiments. As a result, the PV-side current reference is selected as the final current reference for the dc current control, and the resultant dc current does not change in the experiments.

Fig. 8(c) shows the experimental waveforms of the proposed converter under a dynamic state with a leading power factor control (PF = 0.95 leading). Before the leading power factor control, the converter is operating with a unity power factor. Once the leading power factor control is enabled, both the phase angle and magnitude of the grid current change. In addition, the dc current (i_{dc}) increases from 6 to 7 A, and this is because the grid-side current reference is larger than that of the PV-side one and is higher than that under both the unity power factor and lagging power factor. v_{dc1} and v_{dc2} reduce accordingly to ensure that the real power remains unchanged.

Fig. 8(d) shows the experimental waveforms of the proposed converter under a dynamic state with mismatch/fault. The second PV-side converter is bypassed at a given time instant by setting its duty cycle to zero. This can simulate a solar mismatch, parameter mismatch, and a fault of the PV converter in practice. It is worth noting that the dc current reference is still equal to 6 A. This is because the reference determined by the left healthy PV-side converter is still greater than the grid-side one. Therefore, the dc current is controlled to be 6 A in the process. Second, the output voltage of the left healthy PV-side converter (v_{dc1}) is increased

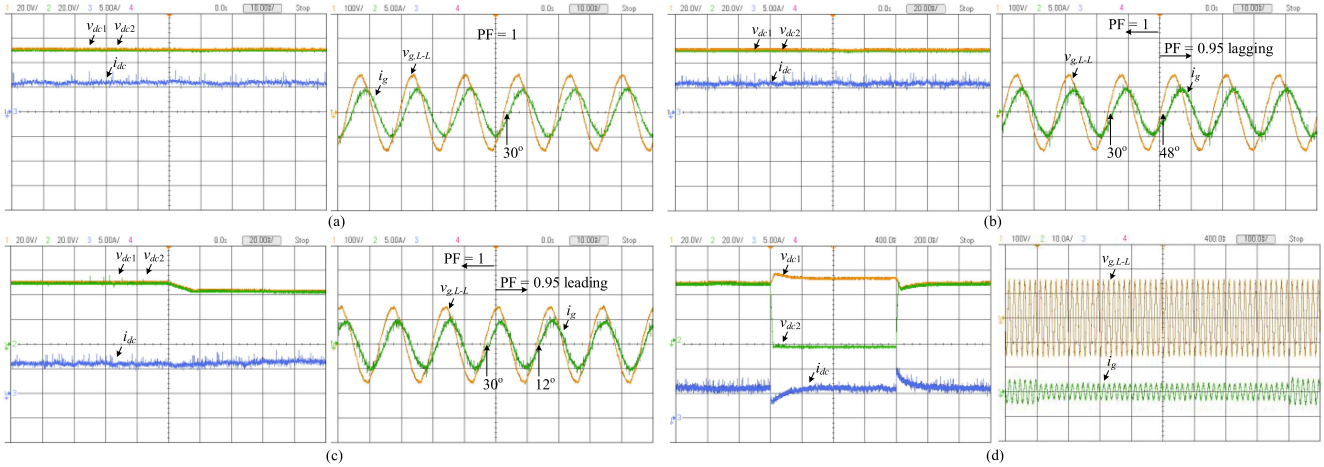

Fig. 8. Experimental waveforms of the converter under rated conditions. (a) Steady state under rated conditions. (b) Dynamic state under lagging power factor control. (c) Dynamic state under leading power factor control. (d) Dynamic state under mismatch/fault.

slightly and this is due to the increase of the diode rectifier output voltage under light load. A similar process repeats when the bypassed PV-side converter is reactivated later.

V. Conclusion

A practical CSI-based converter is proposed for high-power MV PV systems. In addition to eliminating the LFT used in the existing high-power MV PV systems, it also addresses the challenges faced by the CHB- and MMC-based converters, such as the power imbalance, parameter mismatch, overrating, and redundancy design. In addition, it features reliable short-circuit protection, high scalability, simple, and well-proven converters. Both simulations and experiments have been done and verified the performance of the proposed converter. It has shown that the proposed converter is practical and a good candidate for the high-power MV solar systems.

References

[1] M. Malinowski, J. I. Leon, and H. Abu-Rub, "Solar photovoltaic and thermal energy systems: Current technology and future trends," *Proc. IEEE*, vol. 105, no. 11, pp. 2132–2146, Nov. 2017.

[2] Y. Shi, R. Li, Y. Xue, and H. Li, "High-frequency-link-based grid-tied PV system with small dc-link capacitor and low-frequency ripple-free maximum power point tracking," *IEEE Trans. Power Electron.*, vol. 31, no. 1, pp. 328–339, Jan. 2016.

[3] F. V. Amaral, T. M. Parreiras, G. C. Lobato, A. A. P. Machado, I. A. Pires, and B. de Jesus Cardoso Filho, "Operation of a grid-tied cascaded multilevel converter based on a forward solid-state transformer under unbalanced PV power generation," *IEEE Trans. Ind. Appl.*, vol. 54, no. 5, pp. 5493–5503, Sep./Oct. 2018.

[4] Y. Yu, G. Konstantinou, B. Hredzak, and V. G. Agelidis, "Power balance optimization of cascaded H-bridge multilevel converters for large-scale photovoltaic integration," *IEEE Trans. Power Electron.*, vol. 31, no. 2, pp. 1108–1120, Feb. 2016.

[5] Y. Yu, G. Konstantinou, C. D. Townsend, R. P. Aguilera, and V. G. Agelidis, "Delta-connected cascaded H-bridge multilevel converters for large-scale photovoltaic grid integration," *IEEE Trans. Ind. Electron.*, vol. 64, no. 11, pp. 8877–8886, Nov. 2017.

[6] P. Sochor and H. Akagi, "Theoretical and experimental comparison between phase-shifted PWM and level-shifted PWM in a modular multilevel SDBC inverter for utility-scale photovoltaic applications," *IEEE Trans. Ind. Appl.*, vol. 53, no. 5, pp. 4695–4707, Sep./Oct. 2017.

[7] C. D. Townsend, Y. Yu, G. Konstantinou, and V. G. Agelidis, "Cascaded H-bridge multilevel PV topology for alleviation of per-phase power imbalances and reduction of second harmonic voltage ripple," *IEEE Trans. Power Electron.*, vol. 31, no. 8, pp. 5574–5586, Aug. 2016.

[8] C. Wang, K. Zhang, J. Xiong, Y. Xue, and W. Liu, "A coordinated compensation strategy for module mismatch of CHB-PV systems based on improved LS-PWM and reactive power injection," *IEEE Trans. Ind. Electron.*, vol. 66, no. 4, pp. 2825–2836, Apr. 2019.

[9] T. Zhao, X. Zhang, W. Mao, F. Wang, J. Xu, and Y. Gu, "A modified hybrid modulation strategy for suppressing dc voltage fluctuation of cascaded H-bridge photovoltaic inverter," *IEEE Trans. Ind. Electron.*, vol. 65, no. 5, pp. 3932–3941, May 2018.

[10] P. M. Lingom, J. Song-Manguelle, D. L. Mon-Nzongo, R. C. C. Flesch, and T. Jin, "Analysis and control of PV cascaded H-bridge multilevel inverter with failed cells and changing meteorological conditions," *IEEE Trans. Power Electron.*, vol. 36, no. 2, pp. 1777–1789, Feb. 2021.

[11] L. Liu, H. Li, Y. Xue, and W. Liu, "Decoupled active and reactive power control for large-scale grid-connected photovoltaic systems using cascaded modular multilevel converters," *IEEE Trans. Power Electron.*, vol. 30, no. 1, pp. 176–187, Jan. 2015.

[12] Y. Ko, M. Andresen, K. Wang, and M. Liserre, "Modulation for cascaded multilevel converters in PV applications with high input power imbalance," *IEEE Trans. Power Electron.*, vol. 36, no. 9, pp. 10866–10878, Sep. 2021.

[13] R. H. Cuzmar, J. Pereda, and R. P. Aguilera, "Phase-shifted model predictive control to achieve power balance of CHB converters for large-scale photovoltaic integration," *IEEE Trans. Ind. Electron.*, vol. 68, no. 10, pp. 9619–9629, Oct. 2021.

[14] L. Liu, H. Li, Y. Xue, and W. Liu, "Reactive power compensation and optimization strategy for grid-interactive cascaded photovoltaic systems," *IEEE Trans. Power Electron.*, vol. 30, no. 1, pp. 188–202, Jan. 2015.

[15] A. M. Mahfuz-Ur-Rahman, M. R. Islam, K. M. Muttaqi, and D. Sutanto, "A magnetic-linked multilevel active neutral point clamped converter with an advanced switching technique for grid integration of solar photovoltaic systems," *IEEE Trans. Ind. Appl.*, vol. 56, no. 2, pp. 1990–2000, Mar./Apr. 2020.

[16] M. R. Islam, A. M. Mahfuz-Ur-Rahman, M. M. Islam, Y. G. Guo, and J. G. Zhu, "Modular medium-voltage grid-connected converter with improved switching techniques for solar photovoltaic systems," *IEEE Trans. Ind. Electron.*, vol. 64, no. 11, pp. 8887–8896, Nov. 2017.

[17] S. Essakiappan, H. S. Krishnamoorthy, P. Enjeti, R. S. Balog, and S. Ahmed, "Multilevel medium-frequency link inverter for utility scale photovoltaic integration," *IEEE Trans. Power Electron.*, vol. 30, no. 7, pp. 3674–3684, Jul. 2015.

[18] M. R. Islam, Y. Guo, and J. Zhu, "A high-frequency link multilevel cascaded medium-voltage converter for direct grid integration of renewable energy systems," *IEEE Trans. Power Electron.*, vol. 29, no. 8, pp. 4167–4182, Aug. 2014.

[19] C. D. Fuentes, C. A. Rojas, H. Renaudineau, S. Kouro, M. A. Perez, and T. Meynard, "Experimental validation of a single dc bus cascaded H-bridge multilevel inverter for multistring photovoltaic systems," *IEEE Trans. Ind. Electron.*, vol. 64, no. 2, pp. 930–934, Feb. 2017.
[20] S. Kouro, C. Fuentes, M. Perez, and J. Rodriguez, "Single dc-link cascaded H-bridge multilevel multistring photovoltaic energy conversion system with inherent balanced operation," in *Proc. 38th Annu. Conf. IEEE Ind. Electron. Soc.*, 2012, pp. 4998–5005.
[21] M. Wang et al., "Module power balance control strategy for three-phase cascaded H-bridge PV inverter under unbalanced grid voltage condition," *IEEE J. Emerg. Sel. Topics Power Electron.*, vol. 9, no. 5, pp. 5657–5671, Oct. 2021.
[22] T. Zhao and D. Chen, "Analysis and suppression of active power backflow of three-phase common dc-bus cascaded H-bridge PV grid-connected inverter during LVRT," *IEEE J. Emerg. Sel. Topics Power Electron.*, vol. 10, no. 1, pp. 745–759, Feb. 2022.
[23] H. Bayat and A. Yazdani, "A power mismatch elimination strategy for an MMC-based photovoltaic system," *IEEE Trans. Energy Convers.*, vol. 33, no. 3, pp. 1519–1528, Sep. 2018.
[24] S. Rivera, B. Wu, R. Lizana, S. Kouro, M. Perez, and J. Rodriguez, "Modular multilevel converter for large-scale multistring photovoltaic energy conversion system," in *Proc. IEEE Energy Convers. Congr. Expo.*, 2013, pp. 1941–1946.
[25] Y. Liu, H. Abu-Rub, and B. Ge, "Front-end isolated quasi-Z-source dc–dc converter modules in series for high-power photovoltaic systems—Part I: Configuration, operation, and evaluation," *IEEE Trans. Ind. Electron.*, vol. 64, no. 1, pp. 347–358, Jan. 2017.
[26] X. Li, M. Zhu, M. Su, J. Ma, Y. Li, and X. Cai, "Input-independent and output-series connected modular dc–dc converter with intermodule power balancing units for MVdc integration of distributed PV," *IEEE Trans. Power Electron.*, vol. 35, no. 2, pp. 1622–1636, Feb. 2020.
[27] X. Diao, F. Liu, Y. Song, M. Xu, Y. Zhuang, and X. Zha, "A novel fault ride-through topology with high efficiency and fast fault clearing capability for MVdc PV system," *IEEE Trans. Ind. Electron.*, to be published, doi: 10.1109/TIE.2022.3156040.
[28] J. Liu, K. Wang, Z. Zheng, C. Li, and Y. Li, "A dual-active-clamp quasi-resonant isolated boost converter for PV integration to medium-voltage dc grids," *IEEE J. Emerg. Sel. Topics Power Electron.*, vol. 8, no. 4, pp. 3444–3456, Dec. 2020.
[29] F. M. Alhuwaishel, A. K. Allehyani, S. A. S. Al-Obaidi, and P. N. Enjeti, "A medium-voltage dc-collection grid for large-scale PV power plants with interleaved modular multilevel converter," *IEEE J. Emerg. Sel. Topics Power Electron.*, vol. 8, no. 4, pp. 3434–3443, Dec. 2020.
[30] Y. Zhuang et al., "A multiport modular dc–dc converter with low-loss series LC power balancing unit for MVDC interface of distributed photovoltaics," *IEEE Trans. Power Electron.*, vol. 36, no. 7, pp. 7736–7749, Jul. 2021.
[31] O. Khan, W. Xiao, and M. S. E. Moursi, "A new PV system configuration based on submodule integrated converters," *IEEE Trans. Power Electron.*, vol. 32, no. 5, pp. 3278–3284, May 2017.
[32] A. I. Elsanabary, G. Konstantinou, S. Mekhilef, C. D. Townsend, M. Seyedmahmoudian, and A. Stojcevski, "Medium voltage large-scale grid-connected photovoltaic systems using cascaded H-bridge and modular multilevel converters: A review," *IEEE Access*, vol. 8, pp. 223686–223699, 2020.
[33] M. Rabiul Islam, A. M. Mahfuz-Ur-Rahman, K. M. Muttaqi, and D. Sutanto, "State-of-the-art of the medium-voltage power converter technologies for grid integration of solar photovoltaic power plants," *IEEE Trans. Energy Convers.*, vol. 34, no. 1, pp. 372–384, Mar. 2019.
[34] B. Wu and M. Narimani, *High-Power Converters and AC Drives*. New York, NY, USA: Wiley, 2017.
[35] J. He, Q. Li, H. Wang, Y. Lyu, H. Jia, and C. Wang, "SVM strategies for simultaneous common-mode voltage reduction and dc current balancing in parallel current source converters," *IEEE Trans. Power Electron.*, vol. 33, no. 10, pp. 8859–8871, Oct. 2018.
[36] X. Guo, D. Xu, J. M. Guerrero, and B. Wu, "Space vector modulation for dc-link current ripple reduction in back-to-back current-source converters for microgrid applications," *IEEE Trans. Ind. Electron.*, vol. 62, no. 10, pp. 6008–6013, Oct. 2015.
[37] P. Liu, Z. Wang, Q. Song, Y. Xu, and M. Cheng, "Optimized SVM and remedial control strategy for cascaded current-source-converters-based dual three-phase PMSM drives system," *IEEE Trans. Power Electron.*, vol. 35, no. 6, pp. 6153–6164, Jun. 2020.
[38] L. Ming, W. Ding, P. C. Loh, and Z. Xin, "A direct carrier-based modulation scheme with full index range for dc-link current ripple mitigation of a current source converter," *IEEE Trans. Ind. Electron.*, vol. 69, no. 1, pp. 452–462, Jan. 2022.
[39] Z. Bai, H. Ma, D. Xu, B. Wu, Y. Fang, and Y. Yao, "Resonance damping and harmonic suppression for grid-connected current-source converter," *IEEE Trans. Ind. Electron.*, vol. 61, no. 7, pp. 3146–3154, Jul. 2014.
[40] B. Wu, Y. Lang, N. Zargari, and S. Kouro, *Power Conversion and Control of Wind Energy Systems*. New York, NY, USA: Wiley, 2011.
[41] T. M. Jahns, B. Sarlioglu, and J. W. Kolar, "Preparing for the opportunities and challenges of WBG-based motor drives," in *Proc. IEEE Energy Convers. Congr. Expo.*, Washington, DC, USA, 2020.

Ling Xing received the B.Sc. degree from the Harbin Institute of Technology, Harbin, China, in 2009, and the M.A.Sc. degree from Xi'an Jiaotong University, Xi'an, China, in 2012, both in electrical engineering. She is currently working toward the Ph.D. degree in power engineering with the Department of Electrical and Computer Engineering, University of Alberta, Edmonton, AB, Canada.

Her research interest includes high-power converters in renewable energy systems.

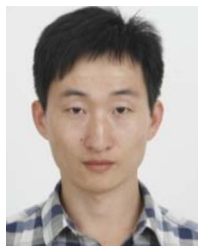

Qiang Wei (Senior Member, IEEE) received the B.Sc. degree from the Henan University of Science and Technology, Luoyang, China, in 2008, the M.A.Sc. degree from Xi'an Jiaotong University, Xi'an, China, in 2012, and the Ph.D. degree from Ryerson University, Toronto, ON, Canada, in 2017, all in electrical engineering.

From 2012 to 2014, he was with Delta Power Electronics, Nanjing, China, as an R&D Engineer. In 2018, he joined Lakehead University, Thunder Bay, ON, Canada, where he is currently an Assistant Professor. His research is focused on innovative power conversions and controls for high-power applications, such as renewable energies, drives, and electric vehicles.

Yunwei Li (Fellow, IEEE) received the B.Sc. degree in electrical engineering from Tianjin University, Tianjin, China, in 2002, and the Ph.D. degree in electrical engineering from Nanyang Technological University, Singapore, in 2006.

In 2005, he was a Visiting Scholar with Aalborg University, Aalborg, Denmark. From 2006 to 2007, he was a Postdoctoral Research Fellow with Ryerson University, Toronto, ON, Canada. In 2007, he also worked with Rockwell Automation Canada before he joined the University of Alberta, Edmonton, AB, Canada, in the same year. Since then, he has been with the University of Alberta, where he is currently a Professor and an Acting Department Chair. His research interests include distributed generation, microgrid, renewable energy, high-power converters, and electric motor drives.

Dr. Li was the recipient of the Richard M. Bass Outstanding Young Power Electronics Engineer Award from IEEE Power Electronics Society (PELS) in 2013. He is an Editor-in-Chief for IEEE TRANSACTIONS ON POWER ELECTRONICS. Prior to that, he was an Associate Editor for IEEE TRANSACTIONS ON POWER ELECTRONICS, IEEE TRANSACTIONS ON INDUSTRIAL ELECTRONICS, IEEE TRANSACTIONS ON SMART GRID, and *IEEE Journal of Emerging and Selected Topics in Power Electronics*. He served as the General Chair of IEEE Energy Conversion Congress of Exposition in 2020. He is the AdCom Member at Large for IEEE PELS from 2021 to 2023. He is recognized as a Highly Cited Researcher by the Web of Science Group.